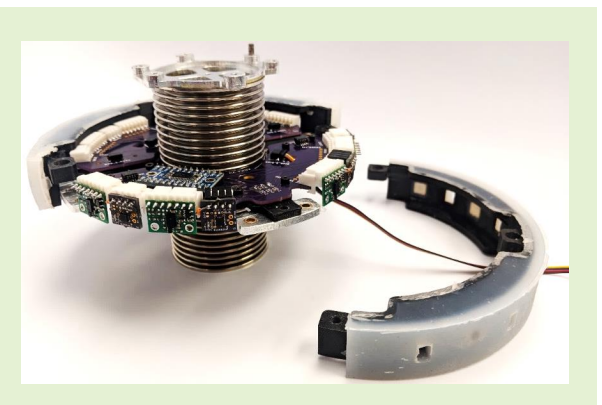


A Multi-Modal Sensor Array for Human-Robot Interaction and Confined Spaces Exploration Using Continuum Robots

Colette Abah, *Student Member, IEEE*, Andrew L. Orekhov, Garrison L. H. Johnston, Nabil Simaan[†], *Fellow, IEEE*

Abstract—Safe human-robot interaction requires robots endowed with perception. This paper presents the design of a multi-modal sensory array for continuum robots, targeting operation in semi-structured confined spaces with human users. Active safety measures are enabled via sensory arrays capable of simultaneous sensing of proximity, contact, and force. Proximity sensing is achieved using time-of-flight sensors, while contact force is sensed using Hall effect sensors and embedded magnets. The paper presents the design and fabrication of these sensors, the communication protocol and multiplexing scheme used to allow an interactive rate of communication with a high-level controller, and an evaluation of these sensors for actively mapping the shape of the environment and compliance control using gestures and contact with the robot. Characterization of the proximity sensors is presented with considerations of sensitivity to lighting, color, and texture conditions.



Also, characterization of the force sensing is presented. The results show that the multi-modal sensory array can enable pre and post-collision active safety measures and can also enable user interaction with the robot. We believe this new technology allows for increased safety for human-robot interaction in confined and semi-structures spaces due to its demonstrated capabilities of detecting impending collision and mapping the environment along the length of the robot. Future miniaturization of the electronics will also allow possible integration in smaller continuum and soft robots.

Index Terms—Continuum robots, Human-robot interaction, Multi-modal sensing.

I. INTRODUCTION

NDUSTRIAL workers often perform manufacturing, assembly, and maintenance tasks in confined spaces. For example, construction professionals sometimes explore and repair structural, electrical and pipe systems in crawl spaces of homes. Airplane mechanics have to crawl into the wing space to inspect and repair hydraulic leaks or fuel tanks. Pipeline workers have to inspect and service storage tanks and large pipes from within. These working conditions put them at risk for work-related musculoskeletal disorders due to sustained non-ergonomic postures [1].

Robotic assistance can alleviate this burden by supporting loads and performing repetitive tasks. This working model

† Corresponding author

The authors are from the Department of Mechanical Engineering, Vanderbilt University, Nashville, TN 37235, USA (Email:{c.abah, andrew.orekhov, garrison.l.johnston, nabil.simaan}@vanderbilt.edu)

This work was supported by NSF award #1734461 and by Vanderbilt University internal funds. A. Orekhov was supported by the NSF Graduate Research Fellowship under #DGE-1445197. C. Abah was partly supported by National Institutes of Health (NIH) award T32-EB021937 of the National Institute of Biomedical Imaging and Bioengineering.

The authors thank Lauren Howard and Sina Ghandi for their contributions to the Teensynet PCB design and the speed characterization experiment, respectively.

has become commonplace in open and structured manufacturing environments, where robots are used both autonomously and in close collaboration with workers [2]–[4]. However, collaborative manufacturing in confined spaces demands new cooperation modes with levels of dexterity, sensing, and safety that exceed the capabilities of existing robotic systems.

There are three viable approaches for robot deployment in confined spaces: a) full autonomy, b) telemanipulation or ex situ collaboration, and c) in situ human-robot collaboration. Full autonomy requires precise knowledge of the environment and reduces the repertoire of available tasks to simple, preplanned tasks. Telemanipulation enables the user to control the robot from outside the confined space, but may not be suitable for applications that require complex manipulation tasks or human sensory presence for quality control. Additionally, most applications that would require robot assistance within a confined space involve operation within semi-structured environments where the basic geometry is known based on the nominal manufacturing plan, but the actual environment differs from this a priori plan due to manual customizations (e.g. passing new wire harnesses, pipes and air conditioning ducts). In situ human-robot collaboration overcomes the aforementioned limitations by providing robotic assistance for loadbearing and repetitive tasks while keeping the human on site to perform complex tasks or manual customizations.

Thanks to their distal actuation, load bearing capabilities, and inherent compliance (passive safety), continuum robots [5] are well suited for deep reach within confined spaces with a co-located human. These robots include serially-stacked segments with each segment comprised from a base disk, an end disk, spacer disks, a central backbone, and tendons or secondary backbones circumferentially distributed around the central backbone and used for actuation. This robot architecture offers the advantage of reduced moving mass since they can be actuated using cables while maintaining the actuators at the base. To further increase the robot situational awareness, and thus ensure the safety of the collocated human, these robots must be augmented with the ability to a) map their environment, b) sense proximity to neighboring objects, and c) detect and localize contacts along their lengths and circumferences. In situ Collaborative Robots (ISCRs) are a novel class of continuum robots that meet these functional requirements.

The literature on sensing methods for continuum robots is extensive. Most works have focused on estimation of the wrench at the end effector by measuring load on actuation lines [6], [7], measuring deflection from equilibrium position [8]–[11], or by integrating Fiber-Bragg Gratings sensors [12]– [14]. In [15] and [16], a kinematics-based method for contact detection and localization along a multi-segment continuum robot was investigated. One limitation of this work was that while external wrenches applied on separate segments could be detected and localized, multiple contacts along a single segment could be detected but not localized. Chen et al. [17] expanded and adapted this kinematics-based approach for contact detection on pneumatic bellow actuators. Nevertheless, none of these methods are sufficient for in situ human robot collaboration, as this application requires contact detection and localization along the full body of the robot. Furthermore, this application requires the integration of additional sensing modalities for force estimation and proximity sensing.

Sensor arrays and robotic skins for whole body sensing have received significant research interest in the past few decades, as surveyed in [18] and [19]. Several works on multi-modal sensing skins, including various combinations of proximity sensing, contact detection, and force sensing, have been published in the context of rigid link robots [20]–[22] and soft robots [23]–[25]. In [26], the authors present whole-body proximity sensing for human-robot interaction with rigid link robots. However, the integration of multi-modal sensing within the structure of a continuum robot has not previously been considered.

The contribution of this paper is in presenting the first case of continuum robots capable of environment shape mapping, contact detection, and force sensing, using distributed sensory disk units (SDUs) along their length. A preliminary design of these novel SDUs was presented in [27], but was limited to presenting the design concept of a single SDU and the validation of its potential use on a PUMA560 robot. Relative to our prior work, this work presents a polished and ruggedized redesign of the SDU, along with details of the

fabrication process, electronics, communication, integration of these SDUs on a continuum robot segment, and validation of mapping capabilities of a continuum robot using these SDUs. We also present the use of these sensors for contact detection and localization, force sensing, and user interaction using admittance control. All of these new sensory capabilities can open a new horizon for the design and use of continuum robots for human-robot interaction and exploration of unstructured environments.

The rest of the paper is structured as follows: First, we detail the design specifications and fabrication procedure for the SDU in Section II. Next, we present the characterization and calibration of the different sensing modalities within the SDU in Section III. Finally, we integrate the SDU within a continuum robot and demonstrate mapping of a confined space and human-robot interaction under complaint motion control in Sections IV and V, respectively.

II. DESIGN AND FABRICATION

The overarching goal of this research is to enable safe human-robot collaboration in semi-structured confined spaces. To achieve this goal, the ISCR must be endowed with whole-body situational awareness in order to a) map the confined space to update an *a priori* model of the environment, b) detect approaching objects, c) detect and localize contact along its body, and d) measure applied external force along its body. In addition, these sensing modalities must seamlessly integrate within the structure of the continuum robot without adding bulk or excess cost.

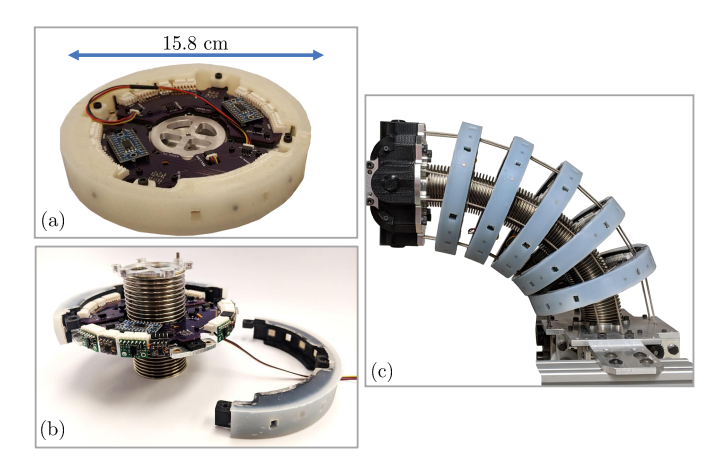


Fig. 1: (a) Multi-modal sensing disk unit (SDU) with proximity sensing, mapping, localized contact detection, and force sensing capabilities. (b) Section view of the SDU prototype, showing integrated Time-of-flight sensors, Hall effect sensors, and custom multiplexer PCBs. (c) SDUs integrated into the structure of a continuum robot for augmented robot situational awareness.

Given these design specifications, we propose an array of multi-modal sensing disk units - SDUs (Fig. 1) that serve the dual purpose of sensing elements for whole-body situational awareness and spacer disks for the continuum robot. Spacer disks are passive structural elements on which the central backbone of a continuum robot is mounted and through which tendons slide to achieve controlled bending in different planes [5], [28]. Fig. 1-(c) shows an overview of the proposed embodiment: a one-segment continuum robot with an array

of five SDUs integrated within its structure and separated by metallic bellows.

Figure 2 presents a detailed view of the internal structure and components of an SDU. Each SDU includes eight time-of-flight (ToF) sensors, eight Hall effect sensors, and eight embedded magnets distributed around its circumference.

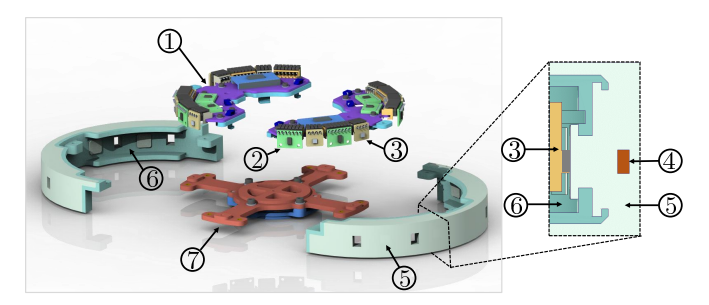


Fig. 2: The SDU includes two custom PCBs ① for multiplexed I²C communication between eight time-of-flight (ToF) sensors ②, eight Hall effect sensors ③, and a Teensy microcontroller (not shown). The magnets ④ used for Hall effect sensing are embedded within a silicone sleeve ⑤. This sleeve is overmolded on a 3D-printed half disk cover ⑥ that encases the SDU. These components are mounted onto a core aluminum disk ⑦, for easy integration within a continuum robot.

A. Time of Flight Sensors

The ToF sensors (STMicroelectronics VL6180X) compute the absolute distance to the nearest object by measuring the time the light takes to travel to the object and reflect back to the sensor. Distributed along the surface of the continuum robot, these sensors enable proximity sensing to detect an approaching object and obtain a point cloud map of the environment. While the density of the map obtained is limited by the physical distribution of the sensors on the robot, a denser map can be obtained by collecting points as the robot is moving or by implementing a control mode in which the continuum robot rotates about its central backbone as presented in [29]. We selected ToF sensors with 0-100mm range to be able to accurately predict onset of contact with a human or an object along the body of the continuum robot. Longer range ToF sensors (e.g. VL53L0X) have been considered, but while they increase the range of detectable objects, they are less accurate for short range interactions. Nevertheless, given that their pinout is identical to our current ToF sensors, these sensor models can be easily integrated into the current setup for mixed range proximity sensing and mapping.

B. Hall Effect Sensors

The Hall effect sensors (Melexis, MLX90393) measure magnetic flux density along their three orthogonal axes of symmetry. To use these sensors for force measurements, we followed the working principle described in [30] and illustrated in the inset of Fig. 2. For each Hall effect sensor, there is a radially-offset cylindrical magnet (KJ Magnetics, D21B-N52, 3.175 mm diameter, 1.5875 mm thickness) embedded in a silicone sleeve. Any external contact with the sensor disk displaces the magnet within the silicone, thus causing a change

in magnetic flux density, which is detected by the corresponding Hall effect sensor. The uncalibrated measurements can be used as an "on/off" metric for contact detection. Once calibrated with a commercial force sensor, this Hall effect setup can be used as a force sensor. Furthermore, because the sensors are distributed at known locations along the robot, the contact detection and force measurement can be localized. The deformation of the silicone sleeve, caused by the application of an external force, is local and only detectable by the closest Hall sensor. The sensors distribution around the SDU is such that neighboring Hall sensors are separated by at least 30 degrees, i.e. 8.27 cm of arc length.

C. Silicone Sleeve

In addition to housing the magnets for Hall effect sensing, the silicone sleeve protects the robot from harsh interactions with both the environment and the user. The sleeve is casted directly onto each half disk cover (HDC) shown as ⑥ in Fig. 2. Each half disk cover was designed with eight windows that are aligned with each sensor. Four of the windows are dimensioned 6 mm by 8 mm and enable unobstructed ToF sensing. The other four windows are dimensioned 7 mm by 7 mm and are filled with silicone for Hall effect sensing. Furthermore, the HDC has lips (upper and lower) and trapping posts (⑦ in Fig. 2) around its edges that ensure permanent adhesion to the silicone sleeve. This fabrication process is an adaptation of "overmolding", which is a type of in injection molding.

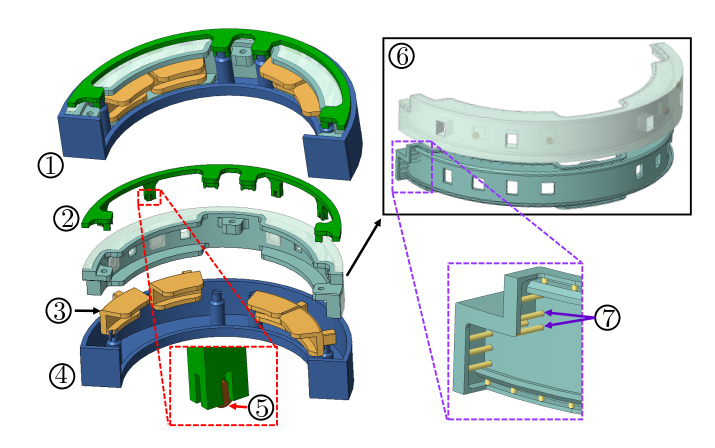


Fig. 3: Mold design for silicone sleeve fabrication: ① Mold components assembled onto the HDCr, ② magnet holder with claws used for repeatable positioning of the four magnets ③. ③ mold inserts (×4) with an extrusion to create windows for time-of-flight sensors and a cavity to create a silicone cushion for the Hall sensor. ④ Outer mold. ⑥ Exploded view of the silicone layer overmolded onto the HDC. Trapping posts ⑦ at the edges of the HDC ensure permanent adhesion of the silicone sleeve.

This sleeve is fabricated by casting liquid silicone rubber (Advanced Reynolds, Dragon Skin FX Pro) into an assembly that includes the HDC and a custom 3D printed mold, as shown in Fig. 3. With a shore 2A hardness, this elastomer is both flexible enough to detect the motion of the embedded magnets, and robust enough to withstand rolling contact with the environment as demonstrated in [27]. The custom mold

includes three main subcomponents: a) an outer mold, b) four mold inserts, and c) a magnet holder.

The casting process is as follows: The mold components are sprayed with mold release for easy demolding. The mold inserts are mounted on the HDC such that each rectangular extrusion fits into a ToF window and each rectangular cavity aligns with the Hall sensor window, as shown in Fig. 3. This sub-assembly is then mounted into the outer mold. The mold cavity is the semi-circular gap between the outer surface of the HDC and the inner surface of the outer mold. Next, the four cylindrical magnets are mounted onto the claws of the magnet holder, with their orientation matching the inlet in Fig. 2. Using the four alignment posts, the magnet holder is assembled onto the outer mold, such that the magnets are suspended within the mold cavity.

The first layer of the two-part liquid silicone (20 g part A, 20 g part B) is mixed, degassed (-30 inHg pressure for three minutes), and poured into the mold cavity until the magnets are fully covered. This layer is then degassed for five additional minutes to remove bubbles formed during the pouring process. The silicone is then left to cure at room temperature for one hour. Once cured, the magnet holder is removed, leaving the magnets trapped in place by the cured silicone.

A second layer of liquid silicone (10 g part A, 10 g part B) is mixed, degassed, and poured to fill the remaining cavity, including the gap left by the magnet holder. Once the second layer is cured, the outer mold and mold inserts are removed, leaving a silicone sleeve overmolded onto the HDC with embedded magnets.

D. Communication Protocol

For communication between the different sensors and a microcontroller, we use the inter-integrated circuit ($\rm I^2C$) communication protocol. This protocol enables communication with up to 128 peripheral devices in a bus configuration, as long as each device has a unique 7-bit address. The data transfer between the controller and peripheral devices occurs at up to 100 kbps in Standard Mode.

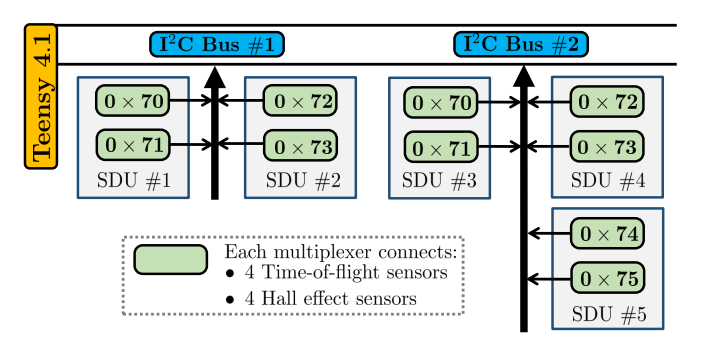


Fig. 4: Strategy for I^2C communication with 40 same-address time-of-flight sensors and 40 same-address Hall sensors, distributed on five disks of a continuum segment.

In our setup, we aim to communicate with 80 sensors (40 ToF and 40 Hall sensors) distributed on five SDUs. The problem is that the ToF sensors all have the same I^2C address (0 \times 29) and the Hall sensors can be hardcoded to one of 16 addresses (0 \times 0C to 0 \times 1B). To bypass the challenge

on non-unique addresses, we use 1-to-8 I²C multiplexers (Texas Instruments, TCA9548A). This multiplexer includes eight bidirectional switches that can be controlled to enable the selection of any individual channel (0 through 7) or combination of channels at high speed (1 GHz). In addition, these multiplexers can be hardwired to eight unique addresses (0x70 to 0x77), thus enabling simultaneous communication with 64 sensors, including duplicate addresses.

With the above solution, even when using eight multiplexers, the design falls short of the desired 80-sensors architecture. To overcome this limitation, we selected a microcontroller with multiple $\rm I^2C$ buses. Our strategy for interfacing with five SDUs is illustrated in Fig. 4. The Teensy 4.1 microcontroller enables the simultaneous use of three $\rm I^2C$ buses, which means that up to 192 sensors (64 sensors \times 3 $\rm I^2C$ buses) can communicate with a single microcontroller. Even though we could have used all three $\rm I^2C$ buses, we reserved the third bus for other sensors we plan to integrate into the segment in the future.

Given this communication architecture, we characterized the speed of sensor data acquisition as a function of the number of active multiplexers (Fig. 5). For a single SDU (i.e. two active multiplexers), data can be collected 20.98 Hz. For the full system (five SDUs or ten multiplexers), data be collected at 4.26 Hz. The bottleneck in sensor data acquisition is the convergence time of the ToF sensors. In the worst case (100 mm and 3% reflectance), the convergence time is 10.73 milliseconds for each sensor. This corresponds to 0.43 seconds or 2.33 Hz for all 40 ToF sensors. We were able to increase the speed to 4.26 Hz by decoupling the initialization and reading sequences for the ToF sensors. For deployment in real Humanrobot interaction scenarios, we will improve the speed of data acquisition by using faster ToF sensing technology when it becomes available. Theoretically, we can speed up the overall acquisition rate for the 40 ToF sensors by adding more microcontrollers instead of relying on a single Teensy board.

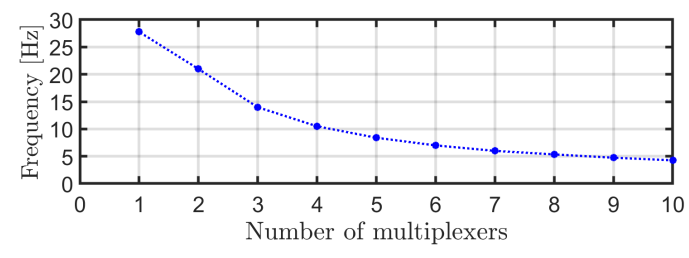


Fig. 5: Frequency of sensor data acquisition as a function of number of active multiplexers (or half disks)

Each SDU includes two custom "half disk" PCBs that serve as breakout boards for each multiplexer (Fig. 6(a)). The sensors are mounted directly on the half disk PCBs using board edge connectors. This architecture facilitates the assembly and troubleshooting of individual sensors, and significantly reduces the number of cables needed. Each half disk PCB includes three QWIIC I^2C connectors (Sparkfun Electronics) that enable daisy-chaining of the half disk PCBs on the same I^2C bus. Each QWIIC connection includes four signals: data (SDA), clock (SCL), power (V_{in}) , and ground (G).

A custom "Teensynet" PCB (Fig. 6(b)) houses the Teensy 4.1 microcontroller and a WIZ850io ethernet module used for User Datagram Protocol (UDP) communication with the robot's main controller. This PCB also breaks out the three I²C buses into individual QWIIC channels with 1 k Ω pull-up resistors on the data and clock lines. The SDU components (ToF sensors, Hall sensors, and multiplexers) and the ethernet module operate at a nominal voltage of 3.3 V, while the microntroller requires 3.6-5.5 V input voltage. To reconcile these voltage requirements and enable the use of a single power supply, this PCB includes a voltage regulator that drops a 5 V input voltage to 3.3 V. Furthermore, the "Teensynet" PCB includes a N-Channel MOSFET that operates as a digital switch to power cycle the SDU sensors.

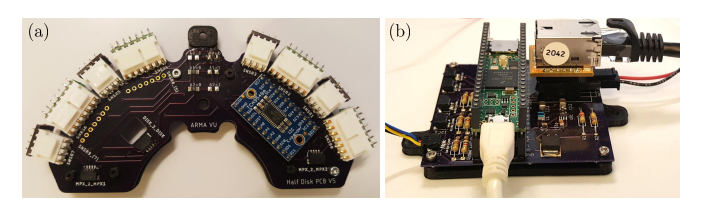


Fig. 6: (a) Half disk custom PCB. (b) Teensynet custom PCB.

III. CHARACTERIZATION AND CALIBRATION

The SDU was characterized and calibrated using the experimental setup shown in Fig. 7. The SDU was mounted on a manual Sherline TM rotary stage, for precise ($\pm 0.1^{\circ}$) angular positioning of the sensor of interest. A custom Cartesian Stage Robot was used to control the motion of an end effector relative to the SDU. This Cartesian robot is comprised of ballscrew-driven Parker TM 404XR series linear stages with 200 mm stroke. Each stage was actuated using a 90 Watt brushed DC motor (Maxon TM RE35 #273754) equipped with a 1000 counts per revolution encoder (Avago technologies #HEDM-5540-B11). A computed torque motion controller was tuned and verified to provide motion accuracy of better than 30 μ m in each direction.

The SDU and rotary stage are positioned at the corner of the Cartesian robot's workspace, in order to maximize usable workspace. The planar pose of the SDU relative to the robot frame was determined as follows: a peg was mounted at the end effector of the Cartesian robot and the robot was jogged until the peg aligned into a matching hole on the SDU. This process was repeated for two angles of the rotary stage ($\theta_{rs} = 0^{\circ}$ and $\theta_{rs} = 90^{\circ}$), thereby allowing the registration of the center of the SDU.

A. Hall Effect Sensing and Force Calibration

The goal of this calibration experiment was to identify the relationship between the magnetic flux density measured by a Hall effect sensor and the magnitude of an external force applied to the SDU. To achieve this calibration, a commercial force sensor (ATI Gamma) with a custom square probe (10 mm \times 10 mm) was mounted as the end effector of the Cartesian Stage Robot. We expect that, when the robot contacts the environment, it will have a contact area larger than the Hall

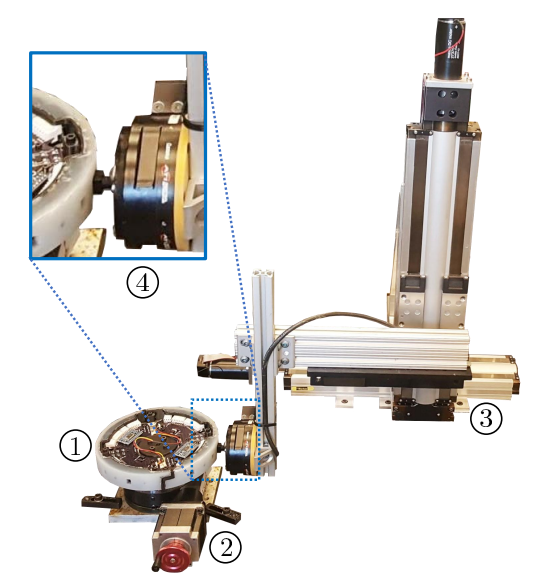


Fig. 7: Experimental setup for SDU characterization: the SDU ① is mounted on a rotary stage ② that controls the orientation of the sensor of interest, relative to a 3-axis Cartesian stage robot ③. An ATI Gamma force sensor ④ is used to probe the touch sensor and provides a ground truth for force measurements

effect sensor windows in the HDC. Thus, the probe was designed to achieve uniform (flat) contact with the silicone sleeve and dimensioned to be bigger than the Hall effect windows in the HDC.

This experiment was performed on all eight Hall effect sensors of a single SDU, and the results informed the calibration of the other Hall sensors on the robot. For each sensor, the rotary stage was used to radially align the target sensor with the normal axis of the force sensor. To achieve vertical alignment between the square probe and the Hall sensor, the Cartesian robot was commanded to position the square probe directly above the SDU. The robot was then jogged slowly until contact was established between the bottom surface of the square probe and the top surface of the SDU. Since the vertical position of the Hall sensor relative to the top of the SDU is known from the CAD model, this information is sufficient to vertically align the probe and the Hall sensor.

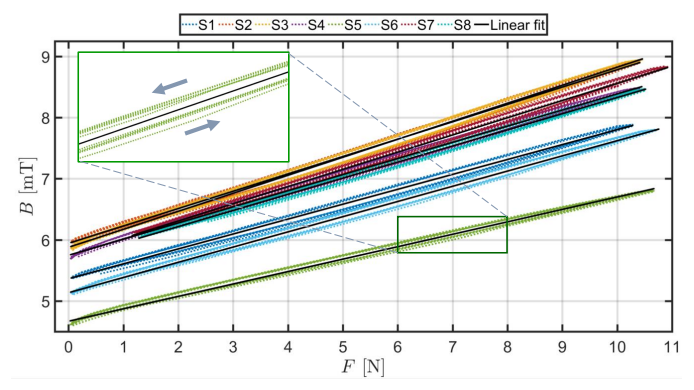


Fig. 8: Force calibration of eight Hall effect sensors around a single SDU

In its initial configuration, the square probe is aligned (radially and vertically) with the Hall sensor, and positioned at the surface of the SDU. The Cartesian robot then moves the

probe into the SDU in increments of $0.1\,\mathrm{mm}$, until a radial force of $10\,\mathrm{N}$ was reached. This force level corresponds with $0.1\,\mathrm{MPa}$ contact pressure, which roughly translates to $82.25\,\mathrm{N}$ contact force between the SDU and a flat surface, with contact area approximating $23.5\,\mathrm{mm} \times 35\,\mathrm{mm}$. Once the $10\,\mathrm{N}$ force threshold is reached, the robot returns to its starting position, using the same incremental motion in the reverse direction. This trajectory was repeated five times for each Hall sensor.

The data collected includes applied force ${\bf F}$ in Newtons, end effector position ${\bf x}$ in millimeters, and magnetic flux density ${\bf B}$ in milliTeslas. The magnetic flux density data was acquired using the Teensy 4.1 microcontroller and transferred to Simulink Real Time via UDP using the Teensynet PCB.

Fig. 8 shows the force and magnetic flux density raw data, along with the linear fit curves, for eight Hall sensors. The dotted lines show experimental data and solid black lines show the linear fit ${\bf B}^*=\alpha {\bf F}+B_0$ for each sensor, where B_0 is a magnetic flux bias. These results show a linear and repeatable relationship between the magnetic flux density and the force applied. The average slope for these eight sensors $\bar{\alpha}=0.26$ mT/N ± 0.03 mT/N. Moving forward, we will unbias all the Hall sensors at startup, and use the average slope α to convert magnetic flux density into force.

The full scale linearity [31] was calculated for each Hall sensor, using (1). The average full scale linearity error for the eight Hall sensors was $4.47\% \pm 0.57\%$.

$$B-linearity = \frac{max|\mathbf{B} - \mathbf{B}^*|}{\Delta \mathbf{B}} \times 100 \tag{1}$$

where $\Delta \mathbf{B}$ is the range of magnetic flux density measurements. The above linearity data is useful for characterizing the linear model fit to the experimental data. However, if one wishes to use the magnetic flux density \mathbf{B} to sense the force applied, the corresponding model becomes $\mathbf{F}^* = \alpha^{-1}(\mathbf{B} - B_0)$ and the full scale linearity error becomes:

F-linearity =
$$\frac{\max|\mathbf{F} - \mathbf{F}^*|}{\Delta \mathbf{F}} \times 100$$
 (2)

The force linearity calculation yielded $4.52\% \pm 0.56\%$. While this is a relatively large force error, these sensors can still be practical and useful to measure force interactions with the user.

B. Proximity Sensing Characterization

In this characterization experiment, our aim was to determine the dimensions of the ToF detection cones, the distance sensing error, the sensitivity to change in object colors and reflectivity, and the repeatability of measurements across different ToF sensors on the SDU. We utilized the setup shown in Fig. 7, with a Delrin® rod of diameter 50.8 mm mounted as the Cartesian robot's end effector, replacing the force sensor assembly. The rod diameter was chosen to approximate the size of a human wrist, which is the narrowest portion of the human anatomy likely to interact with the robot during a collaborative task. While a finger is narrower than the wrist, it is unlikely that a single finger is detected in isolation, without the rest of the palm.

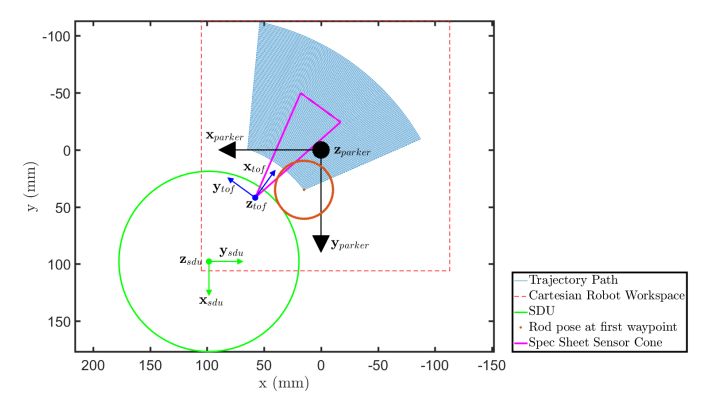


Fig. 9: Trajectory of the Cartesian stage robot during the ToF sensor characterization experiment.

The Cartesian robot's trajectory was chosen such that the Delrin rod sweeps through the detection cone of the target ToF sensor, in increments of 5 mm arch length and 1 mm radius. The VL6180X datasheet reports the ToF detection cone dimensions as $\pm 12.5^{\circ}$ angle and 100 mm height. In its initial configuration, the rod touches the SDU outside the range of the ToF sensor of interest. The rod then sweeps for $\pm 15^{\circ}$ about the central plane of the target ToF sensors, with the radius increasing until the rod is at a radius of 135 mm away from the ToF sensor of interest. At each waypoint along the path, the robot pauses until 20 sensor readings are collected. A top view of this setup is illustrated in Fig. 9.

To determine the sensitivity of the readings to changes in color and reflectivity, the experiment was repeated with three types of Delrin rods: a bare glossy black rod, a rod covered with matte black tape, and a rod covered with a matte light-blue tape. These three tests were performed on two different sensors to validate repeatability of the results across sensors. For each waypoint, the mean sensor ranging error, e was calculated using (3).

$$e = (\|\mathbf{p}_{tof} - \mathbf{p}_{rod}\| - r_{rod}) - \bar{d}$$
 (3)

where \mathbf{p}_{tof} and \mathbf{p}_{rod} are the positions of the sensor and rod in robot frame, r_{rod} is the radius of the rod, and \bar{d} is the mean ranging measurement at the given pose.

Figure 10 reports the results of these experiments in the frame of the ToF sensor (blue frame in Fig. 9). Figure 10(a) and (b) show the ranging error in a 3D and side views, respectively. The figures show that, within the detection cone of the matte black rod, the errors were bounded between 0.01 mm (axis of the cone) and 12.5 mm (edge of the cone). For the glossy black rod, the errors were bounded between 0.019 mm and 15.6 mm. It is also noticeable that the ToF sensors exhibited less error when detecting the matte black surface. Figure 10(c) illustrates the ranging errors on a polar plot. From this figure, the detection cone angle was found to be $\pm 11.9^{\circ}$ for the glossy black rod and $\pm 16.5^{\circ}$ for the matte black rod. Figure 10(d) shows the colorbar plots for the relative error in the ranging value on top. This figure shows that the ToF sensors can detect the rods accurately up to 130 mm, even though their nominal range is 100 mm. These plots also show qualitatively the effects of surface reflectivity on the error. It

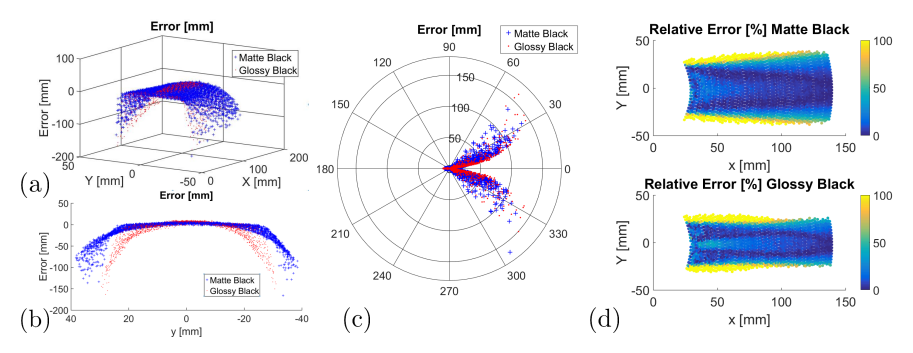


Fig. 10: ToF sensor characterization results: (a) 3D plot of sensor error for matte and glossy rods, (b) side view of 3D sensor error, (c) polar plot of absolute error as a function of line of sight angle of the detected object, (d) relative error colormap. Figure reproduced from [27].

can be seen the glossy reflecting surface decreased the width of the detection cone. The results reported in Fig. 10 are that of one sensor and one rod color. The experiments with the Delrin rod covered with matte blue tape showed similar results and were omitted for space considerations.

IV. Mapping with Continuum Robots

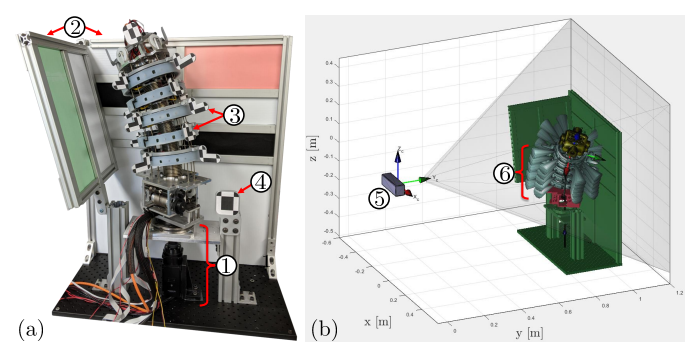


Fig. 11: Mapping experiment: a continuum robot with integrated SDUs is mounted on rotary stage ① and commanded to roll and bend in different configurations in order to obtain a map of a mock confined space ② using the distributed ToF sensors. Custom markers are mounted on each SDU ③ and at the base of the robot ④, and tracked by a ClaronHDTM optical tracker ⑤. The detection cones of the ToF sensors are shown in ⑥.

To illustrate the utility of the SDUs for enabling active mapping using continuum robots, we carried out an experiment using the setup shown in Fig. 11. While a stationary SDU has blind spots due to the spatial allocation of the sensors, the motion SDUs along a continuum robot enables a full sweep of target objects within the workspace of the robot. The experimental setup includes a custom continuum segment with a length of 370 mm and an outside diameter determined by the diameter of the SDUs (158 mm). This continuum segment is meant to be part of a multi-segment continuum robot that will operate in confined spaces. Each continuum segment achieves bending in two perpendicular planes, using an actuation unit at its base. Using coordinated pulling and relaxation of wire ropes, the central backbone is bent to achieve an approximately circular bending shape. To endow the setup with more motion capability for the mapping task, we mounted the continuum segment on a revolute joint that is coaxial with the continuum segment's central backbone. This architecture allows the continuum segment to roll about its central backbone while bending in different planes by using synchronized actuation of its wires, according to the constant-curvature kinematic model presented in [5]. The control code for this trajectory was executed at 100 Hz.

Three markers were affixed around the circumference of each SDU to ensure that at least one marker frame is always detected by the ClaronHDTM H3-50 optical tracker. This tracker allows frame detection with an rms error of 0.2 mm within its workspace. For this experiment, the optical tracker collected frame information at 8.08 Hz.

The robot was placed inside a mock confined space comprised from 80/20 Aluminum extrusions and poster boards partially covered with felt and colored paper. To span the confined space, the robot was commanded to simultaneously bend in a given plane (± 0.02 rad/s), spin to update the orientation of its bending plane ($\pm 0.1 \text{ rad/s}$), and roll about its central backbone (± 0.1 rad/s). During this motion, sensor data from the SDUs is read by the microcontroller, sent to a Robot Operating System (ROS) interface via UDP, published as rostopics, and stored using the rosbag functionality. The motion rates of the robot during the data collection potentially have some effect on the geometry mapping using ToF sensors, because communication with the sensors is executed at 4.26 Hz. The effect of these motions on the resulting map geometry and means to rectify the mapped model will be a subject of future work, and will remain outside the scope of this contribution.

The proximity data is recorded with respect to a frame $\{s\}$ located at the top surface of each ToF sensor and the Micron-Tracker information is used to calculate the transformation between the sensor frame $\{s\}$ and the world coordinate frame $\{0\}$ at the base of the continuum robot (4 in Fig. 11). This transformation is given by:

$${}^{0}\mathbf{H}_{s} = ({}^{c}\mathbf{H}_{0})^{-1} {}^{c}\mathbf{H}_{m}{}^{m}\mathbf{H}_{d}{}^{d}\mathbf{H}_{s} \tag{4}$$

where $\{c\}$ is the frame of MicronTracker camera (5), $\{m\}$ is the frame of the marker on an SDU (3), and $\{d\}$ is the frame at the center of an SDU. Note that ${}^c\mathbf{H}_0$ and ${}^c\mathbf{H}_m$ are obtained from MicronTracker data, while ${}^m\mathbf{H}_d$ and ${}^d\mathbf{H}_s$ are extracted from the CAD model.

A. Ground Truth Map of the Confined Space

A Faro Fusion arm was utilized to obtain the ground truth map of the confined space. First, the Faro hard probe was used

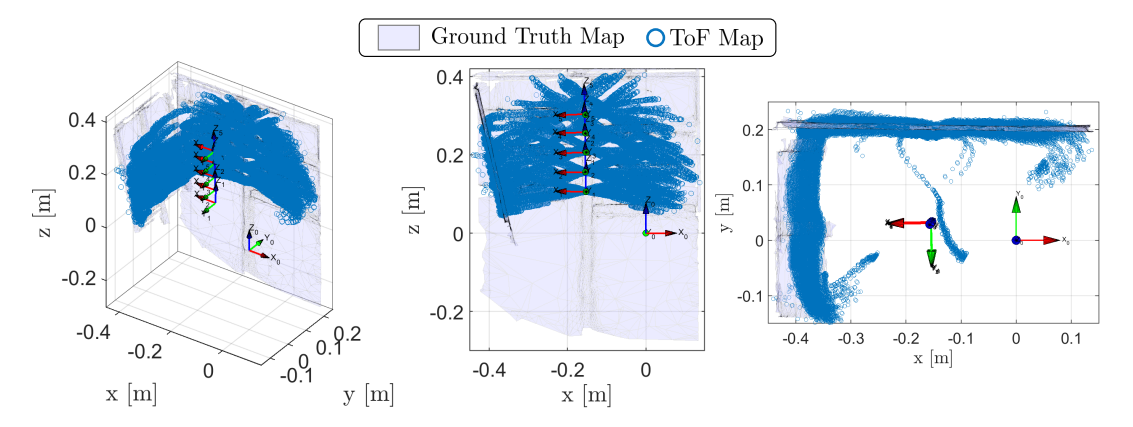


Fig. 12: Mapping results -(a) isometric, (b) front, and (c) top views - showing the ToF map obtained using the SDUs along the continuum robot, along with the ground truth map scanned using a Faro Arm.

to digitize three intersecting planes at the top right corner of the base marker (④ in Fig. 11). The reference frame defined by these three planes served to register the Faro arm to the base frame {0} of the continuum robot. Next, the Faro's laser scan feature was used to digitize the inner surface of the fabricated confined space. The resulting STL model is shown in Fig. 12.

The Faro map consists of four main planes Aluminum Vertical - ALV, poster board vertical - PBV, Aluminum slanted - ALS, and poster board slanted - PBS, with a 9.25 mm offset between the aluminum and poster board surfaces. The normal vectors to these planes were measured from the STL of the Faro scan, relative to the base frame $\{0\}$: $\hat{\mathbf{n}}_1 = [0,1,0]^T$ for the vertical planes and $\hat{\mathbf{n}}_2 = [0.98,0,0.22]^T$ for slanted planes. These four ground truth planes (as shown in Fig. 13) are used to evaluate the mapping performance of the ToF sensors.

B. ToF Map of the Confined Space

The proximity data captured by the ToF sensors during the motion of the continuum robot resulted in an experimental map of the confined space. This map, which we refer to as "ToF map", is illustrated in Fig. 12. We compared the ToF map to the ground truth planes described in the previous section. To do so, we split the raw ToF map into four regions, corresponding to the four ground truth planes. First, we split the ToF map into a vertical set and a slanted set, using MATLAB's pcfitplane, which is a random sample consensus (RANSAC) algorithm that estimates the parameters of the plane for a given point cloud. Additional inputs to this function are the maximum distance from an inlier point to the plane and a reference orientation constraint. We set the maximum allowable distance to be 40 mm and used the normals of confined space walls ($\hat{\mathbf{n}}_1$ and $\hat{\mathbf{n}}_2$) as reference vectors. Next, the resulting two ToF sets are further split into the poster board set and the Aluminum set by projecting onto both planes and electing the closest plane as the parent plane. The resulting four ToF map sets are shown in Fig. 13, along with the parent ground truth planes.

This classification was used to calculate the RMS error, such that the residuals are the orthogonal projection of each point to its parent ground truth plane. The resulting ToF mapping error was 9.73 mm. While a more thorough methodology for quantifying the mapping error could be used by borrowing

from the literature of point cloud to rigid body registration, we believe that such analysis should be carried out after the mapping model rectification has been implemented to counteract the mapping artifacts included by the kinematics of the motion of the SDUs while collecting the ToF data. In addition, the use of the MicronTracker to track the shape of the continuum robot introduces tracking artifacts, due to lighting conditions and the reflectivity of the markers. The video extension shows that in some instances, one of reconstructed SDU frames deviates from the spline of the central backbone. This source of error will be eliminated once the kinematics of the continuum robots are calibrated using integrated shape sensing elements, which will be the subject of future studies with this continuum robot.

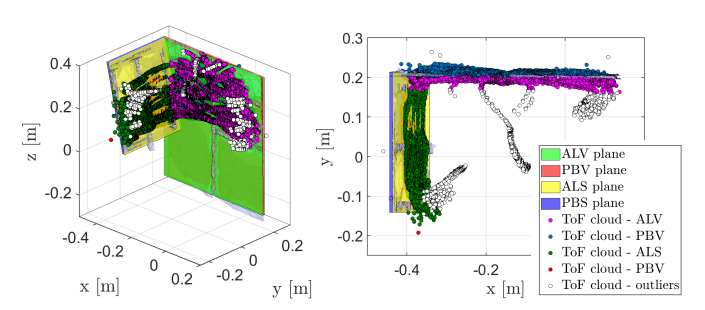


Fig. 13: ToF point clouds sorted by proximity to ground truth (ALV, PBV, ALS, PBS) planes.

V. HUMAN-ROBOT INTERACTION

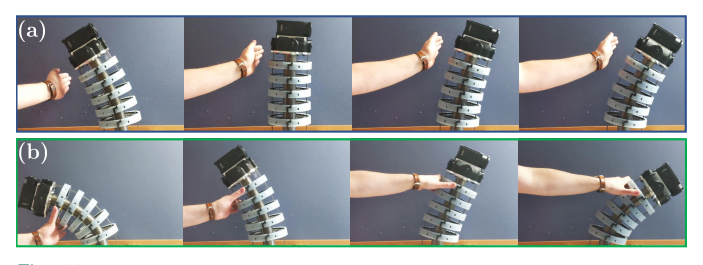


Fig. 14: Video snapshots of two active compliance human-robot interaction modes: (a) Contact-less using time-of-flight sensors (b) Contact-based using Hall effect sensors.

The continuum robot described in Section IV was also used to demonstrate the two modes of human-robot interaction (contact-less and contact-based) supported by the SDUs. For this experiment, the robot was mounted on a static base and sensors from the top SDU were used for active compliance motion control. Multimedia extension I shows these two modes of operation. Also, Fig. 14 shows video snapshots of this multimedia extension.

In Fig. 14a shows the contact-less interaction mode where the robot moves away from a user's hand using the ToF sensors. For this behavior, we selected two ToF sensors on the right and left sides of the segment and commanded the velocity of one motor according to:

$$v_m = \gamma \left(d_r - d_\ell \right) \tag{5}$$

where v_m is the velocity of the motor, γ is a manually-tuned gain, and d_r and d_ℓ are the distances measured with right and left ToF sensors, respectively.

Figure 14b shows the contact-based interaction mode where the robot moves based on sensed contact using the Hall effect sensors. For this behavior, we similarly selected two Hall effect sensors on the right and left sides of the segment and the velocity of the motor is commanded according to:

$$v_m = \gamma \left(\Delta B_{z,r} - \Delta B_{z,\ell} \right) \tag{6}$$

where $\Delta B_{z,r}$ and $\Delta B_{z,\ell}$ are the changes in the magnetic flux density measured along the z axis of the sensors on the right and left sides, respectively.

These simple control laws demonstrate the potential of our proposed multi-modal sensing disks for human-robot interaction along the body of a continuum robot.

VI. DISCUSSION

Table I summarizes the key performance measures of our proposed multi-modal sensing architecture. The proximity data obtained from the distributed ToF sensors resulted in a map of the environment, accurate to 9.73 mm. The accuracy of the mapping was influenced by the ToF sensor data and by latency-induced motion artifacts due to the slow acquisition speed from the optical tracker we used to determine the spatial pose of each SDU. With an acquisition rate of 8.08 Hz, a motion speed of ± 0.1 rad/s, and optical markers located at a radius of 108.5 mm from the central backbone, the latency-induced position uncertainty is 1.343 mm. In the future, we anticipate using real-time shape sensing of the continuum segment to overcome the need for tracking the SDUs. Such shape sensing may be obtained using fiber-Bragg grating curvature sensors.

The mapping error we obtained is also influenced by the low data acquisition speed of the ToF sensors. While one could speed up the overall acquisition rate for a continuum segment to be closer to 20.4 Hz by using individual micro-processors for each SDU, faster ToF sensor technology is needed to allow faster acquisition rates for more accurate mapping and for safer human-robot interaction. Since the uncertainty of mapping depends on the motion being carried out by the robot, future works will need to investigate the effects of the robot's motion on the mapping performance and to optimize the motion of the robot for minimal uncertainty mapping results.

ToF detection error	Matte surface along cone axis: 0.1 mm Matte surface at cone edge: 12.5 mm Glossy surface along cone axis: 0.019 mm Glossy surface at cone edge: 15.6 mm
Hall sensor F-linearity:	$4.52\% \pm 0.56\%$
Communication	1 SDU: 20.4 Hz (ToF & Hall sensors)
Frequency	5 SDUs: 4.26 Hz (ToF & Hall sensors)
Mapping RMSE:	9.73 mm [†]

 $^{^\}dagger$ Result is influenced by 8.08Hz optical tracker acquisition frequency and the motion of the optical markers

TABLE I: Summary of performance characteristics

VII. CONCLUSION

Human-robot collaboration in confined spaces requires the use of continuum robots with whole-body situational awareness. To address this need, we developed sensing disk units (SDUs) that integrate into the body of continuum robots and endow them with a) mapping, b) proximity sensing, c) contact detection and localization, and d) force sensing capabilities. This paper presented the detailed design and fabrication of the SDU components, along with the communication protocol required to interface with an array of SDUs.

Experimental evaluation showed a linear and repeatable relationship between the magnetic flux density and the external force applied, with each Hall effect sensor having its own magnetic flux density bias. Results for the ToF sensors also showed that matte surfaces are detected more accurately and with a wider detection cone than glossy surfaces and that the color of the detected object was not significant.

Finally, a continuum robot with five SDUs was used to demonstrate the utility of whole-body sensing for active mapping and human-robot collaboration. We believe that this work is a significant step towards a novel class of continuum robots that can be deployed in confined spaces, intelligently interact with their environment, and safely assist a co-located worker.

REFERENCES

- M. Lorenzini, W. Kim, E. D. Momi, and A. Ajoudani, "A New Overloading Fatigue Model for Ergonomic Risk Assessment with Application to Human-Robot Collaboration," in 2019 International Conference on Robotics and Automation (ICRA), vol. 25. IEEE, may 2019, pp. 1962

 1968
- [2] M. Zinn, O. Khatib, B. Roth, and J. K. Salisbury, "Playing it safe [human-friendly robots]," *IEEE Robotics & Automation Magazine*, vol. 11, no. 2, pp. 12–21, 2004.
- [3] A. De Luca, A. Albu-Schaffer, S. Haddadin, and G. Hirzinger, "Collision detection and safe reaction with the dlr-iii lightweight manipulator arm," in 2006 IEEE/RSJ International Conference on Intelligent Robots and Systems. IEEE, 2006, pp. 1623–1630.
- [4] R. Bloss, "Collaborative robots are rapidly providing major improvements in productivity, safety, programing ease, portability and cost while addressing many new applications," *Industrial Robot: An International Journal*, vol. 43, no. 5, pp. 463–468, 2016.
- [5] N. Simaan, R. Taylor, and P. Flint, "A dexterous system for laryngeal surgery," in *Robotics and Automation*, 2004. Proceedings. ICRA'04. 2004 IEEE International Conference on, vol. 1. IEEE, 2004, pp. 351– 357
- [6] K. Xu, N. Simaan et al., "An investigation of the intrinsic force sensing capabilities of continuum robots," *IEEE Transactions on Robotics*, vol. 24, no. 3, pp. 576–587, 2008.
- [7] R. Yasin and N. Simaan, "Joint-level force sensing for indirect hybrid force/position control of continuum robots with friction," *The Interna*tional Journal of Robotics Research, vol. 40, no. 4-5, pp. 764–781, 2021.

- [8] D. C. Rucker and R. J. Webster, "Deflection-based force sensing for continuum robots: A probabilistic approach," in *Intelligent Robots and Systems (IROS)*, 2011 IEEE/RSJ International Conference on. IEEE, 2011, pp. 3764–3769.
- [9] W. Wei and N. Simaan, "Modeling, Force Sensing, and Control of Flexible Cannulas for Microstent Delivery," *Journal of Dynamic Systems, Measurement, and Control*, vol. 134, no. 4, p. 041004, 2012.
- [10] S. Hasanzadeh and F. Janabi-Sharifi, "Model-Based Force Estimation for Intracardiac Catheters," *IEEE/ASME Transactions on Mechatronics*, vol. 21, no. 1, pp. 154–162, 2016.
- [11] H. Donat, S. Lilge, J. Burgner-Kahrs, and J. J. Steil, "Estimating Tip Contact Forces for Concentric Tube Continuum Robots Based on Backbone Deflection," *IEEE Transactions on Medical Robotics and Bionics*, vol. 2, no. 4, pp. 619–630, oct 2020.
- [12] R. Xu, A. Yurkewich, and R. V. Patel, "Curvature, torsion, and force sensing in continuum robots using helically wrapped fbg sensors," *IEEE Robotics and Automation Letters*, vol. 1, no. 2, pp. 1052–1059, 2016.
- [13] F. Khan, R. J. Roesthuis, and S. Misra, "Force sensing in continuum manipulators using fiber Bragg grating sensors," in *IEEE International Conference on Intelligent Robots and Systems*, vol. 2017-September. Institute of Electrical and Electronics Engineers Inc., dec 2017, pp. 2531–2536.
- [14] Z. Wu, A. Gao, N. Liu, Z. Jin, and G. Z. Yang, "FBG-Based Triaxial Force Sensor Integrated with an Eccentrically Configured Imaging Probe for Endoluminal Optical Biopsy," in *Proceedings - IEEE International Conference on Robotics and Automation*. Institute of Electrical and Electronics Engineers Inc., may 2020, pp. 1625–1631.
- [15] R. E. Goldman, A. Bajo, and N. Simaan, "Compliant motion control for continuum robots with intrinsic actuation sensing," in *Proceedings - IEEE International Conference on Robotics and Automation*, 2011, pp. 1126–1132.
- [16] A. Bajo and N. Simaan, "Kinematics-based detection and localization of contacts along multisegment continuum robots," *IEEE Transactions* on *Robotics*, vol. 28, no. 2, pp. 291–302, 2012.
- [17] Y. Chen, L. Wang, K. Galloway, I. Godage, N. Simaan, and E. Barth, "Modal-based kinematics and contact detection of soft robots," *Soft Robotics*, 2020.
- [18] D. Silvera-Tawil, D. Rye, and M. Velonaki, "Artificial skin and tactile sensing for socially interactive robots: A review," *Robotics and Au*tonomous Systems, vol. 63, pp. 230–243, 2015.
- [19] Z. Kappassov, J.-A. Corrales, and V. Perdereau, "Tactile sensing in dexterous robot hands," *Robotics and Autonomous Systems*, vol. 74, pp. 195–220, 2015.
- [20] D. Hughes, J. Lammie, and N. Correll, "A robotic skin for collision avoidance and affective touch recognition," *IEEE Robotics and Automa*tion Letters, vol. 3, no. 3, pp. 1386–1393, 2018.
- [21] M. Kaboli, D. Feng, K. Yao, P. Lanillos, and G. Cheng, "A tactile-based framework for active object learning and discrimination using multimodal robotic skin," *IEEE Robotics and Automation Letters*, vol. 2, no. 4, pp. 2143–2150, 2017.
- [22] P. Mittendorfer and G. Cheng, "Humanoid multimodal tactile-sensing modules," *IEEE Transactions on robotics*, vol. 27, no. 3, pp. 401–410, 2011
- [23] R. Patel, R. Cox, and N. Correll, "Integrated proximity, contact and force sensing using elastomer-embedded commodity proximity sensors," *Autonomous Robots*, vol. 42, no. 7, pp. 1443–1458, 2018.
- [24] M. Sohgawa, A. Nozawa, H. Yokoyama, T. Kanashima, M. Okuyama, T. Abe, H. Noma, and T. Azuma, "Multimodal measurement of proximity and touch force by light-and strain-sensitive multifunctional mems sensor," in SENSORS, 2014 IEEE. IEEE, 2014, pp. 1749–1752.
- [25] Y. Yamada, T. Morizono, Y. Umetani, and H. Takahashi, "Highly soft viscoelastic robot skin with a contact object-location-sensing capability," *IEEE Transactions on Industrial electronics*, vol. 52, no. 4, pp. 960–968, 2005.
- [26] Y. Ding and U. Thomas, "Collision avoidance with proximity servoing for redundant serial robot manipulators," in 2020 IEEE International Conference on Robotics and Automation (ICRA), 2020, pp. 10249– 10255.
- [27] C. Abah, A. L. Orekhov, G. L. Johnston, P. Yin, H. Choset, and N. Simaan, "A multi-modal sensor array for safe human-robot interaction and mapping," *Proceedings - IEEE International Conference on Robotics and Automation*, vol. 2019-May, pp. 3768–3774, 2019.
- [28] I. A. Gravagne and I. D. Walker, "Kinematic transformations for remotely-actuated planar continuum robots," in *Robotics and Automa*tion, 2000. Proceedings. ICRA'00. IEEE International Conference on, vol. 1. IEEE, 2000, pp. 19–26.

- [29] N. Simaan, K. Xu, W. Wei, A. Kapoor, P. Kazanzides, R. Taylor, and P. Flint, "Design and integration of a telerobotic system for minimally invasive surgery of the throat," *The International journal of robotics* research, vol. 28, no. 9, pp. 1134–1153, 2009.
- [30] T. Paulino, P. Ribeiro, M. Neto, S. Cardoso, A. Schmitz, J. Santos-Victor, A. Bernardino, and L. Jamone, "Low-cost 3-axis soft tactile sensors for the human-friendly robot vizzy," in *Robotics and Automation (ICRA)*, 2017 IEEE International Conference on. IEEE, 2017, pp. 966–971.
- [31] R. H. Bishop, "The Mechatronics Handbook, Second Edition 2 Volume Set," in *The Mechatronics Handbook, Second Edition - 2 Volume Set*. CRC Press, feb 2002, pp. 18–3.



Colette Abah received her B.S. in mechanical engineering from the Massachusetts Institute of Technology (MIT), Cambridge, MA, USA, in 2015. She was a research fellow at the Wyss Institute at Harvard University, before pursuing a Ph.D. in mechanical engineering at Vanderbilt University, Nashville, TN, USA. She became a Vanderbilt Institute for Surgery and Engineering (VISE) fellow in 2018. Her research interests include design, modelling, control, and sensing of continuum robots and steerable catheters.



Andrew L. Orekhov received the B.S. degree in mechanical engineering from the University of Tennessee, Knoxville, TN, USA, in 2016, and is currently working toward the Ph.D. in mechanical engineering at Vanderbilt University, Nashville, TN, USA. His current research interests include design, modeling, and control of continuum manipulators. He received the NSF Graduate Research Fellowship in 2016.



Garrison L. H. Johnston received his B.S. degree in mechanical engineering from Rensselaer Polytechnic Institute (RPI), Troy, NY, USA, in 2018. He is currently working toward a Ph.D. in mechanical engineering at Vanderbilt University, Nashville, TN, USA. His current research interests include human-robot interaction, robot control, and mechanism design.



Nabil Simaan (F'20) received his Ph.D. degree in mechanical engineering from the Technion—Israel Institute of Technology, Haifa, Israel, in 2002. During 2003, he was a Post-doctoral Research Scientist at Johns Hopkins University National Science Foundation (NSF) ERC-CISST. In 2005, he joined Columbia University, New York, NY. In 2009 he received the NSF Career award for young investigators to design new algorithms and robots for safe interaction with the anatomy. In Fall 2010 he joined

Vanderbilt University. In 2020 he was named an IEEE Fellow for contributions to dexterous continuum robotics. In 2021 he was named ASME Fellow. His research interests include medical robotics, kinematics, robot modeling and control and human-robot interaction.